

Supporting Information for: Spatially Resolved Persistent Photoconductivity in MoS₂–WS₂ Lateral Heterostructures

Samuel Berweger,^{*,†} Hanyu Zhang,[‡] Prasana K. Sahoo,^{*,¶,§} Benjamin M. Kupp,^{||,†} Jeffrey L. Blackburn,[‡] Elisa M. Miller,[‡] Thomas M. Wallis,[†] Dmitri V. Voronine,[¶] Pavel Kabos,[†] and Sanjini U. Nanayakkara^{*,‡}

[†]*Applied Physics Division, National Institute of Standards and Technology, Boulder, CO, 80305, USA*

[‡]*Materials and Chemical Science and Technology Directorate, National Renewable Energy Laboratory, Golden, CO, 80401, USA*

[¶]*Department of Physics, University of South Florida, Tampa, FL, 33620, USA*

[§]*Materials Science Centre, Indian Institute of Technology Kharagpur, Kharagpur, 721302, India*

^{||}*The Pennsylvania State University, University Park, PA, 16802, USA*

E-mail: samuel.berweger@nist.gov; prasana@matsc.iitkgp.ac.in; sanjini.nanayakkara@nrel.gov

Optical Properties

The samples studied in this work were placed on transparent substrates in order to enable through-sample illumination. Due to the resulting reduced optical contrast we compare our flakes with previous work^{1,2} to confirm layer thickness. In Figures S1a and b we show optical micrographs of as-grown MoS₂–WS₂ lateral heterostructure samples on SiO₂/Si with flakes

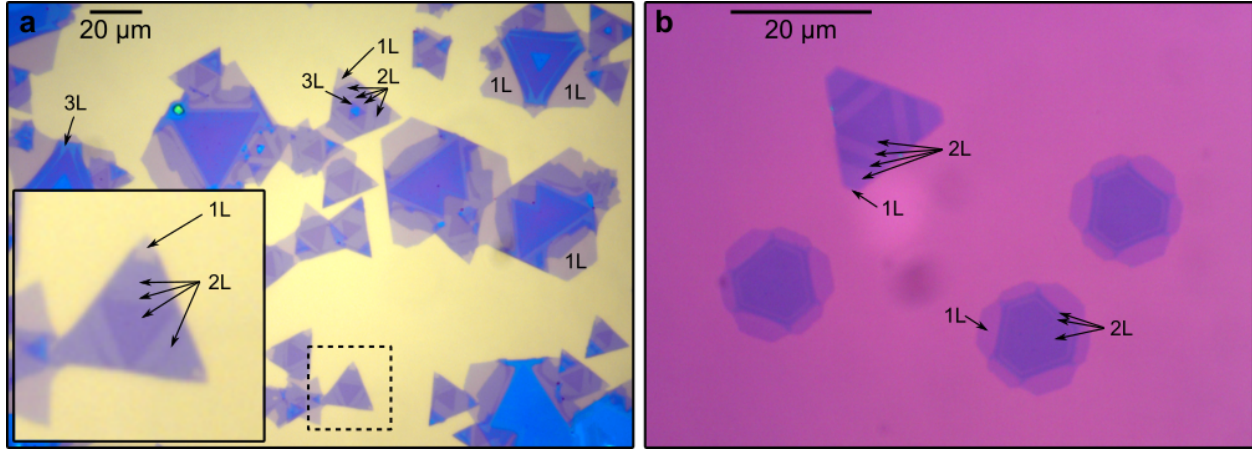


Figure S1: **Optical micrographs of lateral heterostructures.** Optical micrographs of as-grown MoS₂-WS₂ lateral heterostructures on SiO₂/Si substrates showing flakes with morphology similar to flake 1 (a) and flake 2 (b) with thicknesses as indicated.

showing similar morphology to flakes 1 and 2. Layer thicknesses were determined using a combination of Raman Spectroscopy, Photoluminescence, and HAADF-STEM^{1,2} to yield unambiguous layer number determinations as indicated. Contrast differences between a and b are due to different objectives and camera settings used.

Here we also show the expanded set of optical images and PL maps for flakes 1 and 2. In Figure S2a and f are the unmodified optical micrographs of flakes 1 and 2. Figure S2b and g show contrast-optimized and smoothed gray-scale optical micrographs of flakes 1 and 2 to highlight the dark regions visible throughout both flakes. Shown in Fig S2c and h are the spatially resolved PL maps at 1.97 eV with the photon energy at the PL intensity maximum in Fig S2d and i. Two clear regions within the flakes become apparent from comparison of the emission intensities and the emission energies. Within larger regions of the SL WS₂ domains there is a clear correlation between increased emission intensity and an overall blueshift of the emission wavelength, which in many cases originates from the dark regions seen in the optical images. However, a clear blueshift in the emission is also seen at the flake edges, which are all terminated by SL WS₂ and show only weak emission.

Lastly, shown in Fig S2e and j are log scale false color maps of the maximum emission intensity at each spatial pixel. These log scale maps clearly show that the interior ML

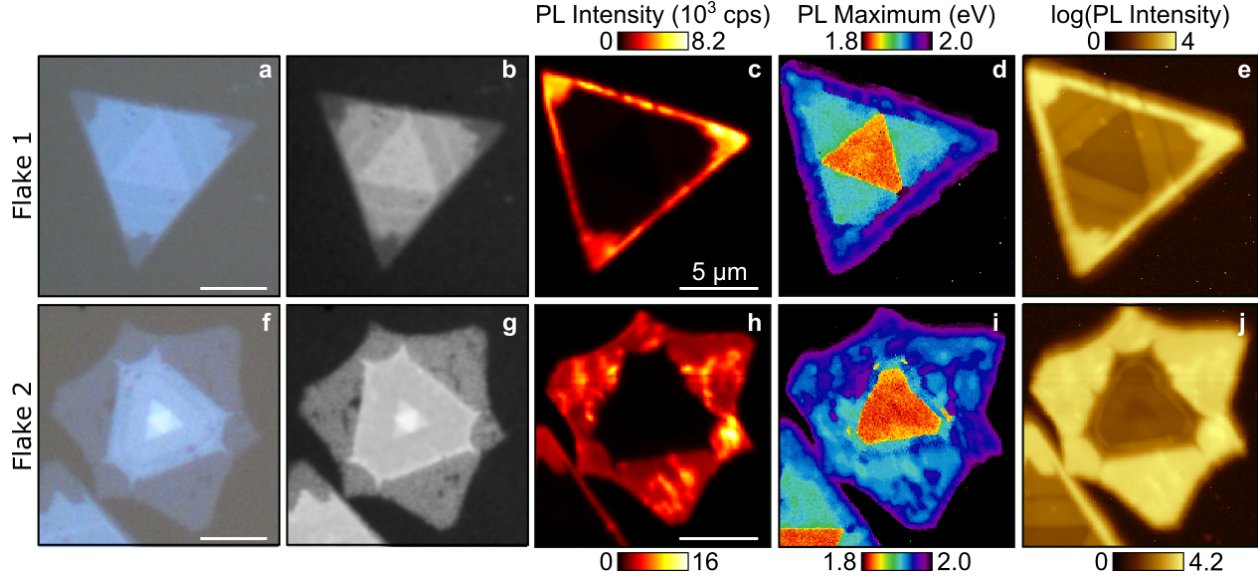


Figure S2: **Optical and PL maps of flakes 1 and 2.** (a) and (f) unmodified optical micrographs of flakes 1 and 2, with contrast-optimized gray-scale versions in (b) and (g), respectively. (c) and (h) the spatially resolved PL maps at 1.97 eV, the photon energy at the emission maximum at each spatial pixel (d) and (i), and a log-scale map of the maximum emission intensity to show variations between the BL MoS₂ and WS₂ domains (e) and (j).

WS₂ and MoS₂ domains are well resolved, with the former showing a uniformly higher peak emission intensity. The log scale maps also clearly show that the edge region PL blueshift corresponds with the reduced PL intensity seen when the far-field laser focus is at the edge of the flake.

Supplementary Sequence

In Figure S3 we show the wavelength-dependent evolution of the photoconductivity for an additional heterostructure flake with a similar internal structure to flake 1. Shown in Figure S3a and b are the contact-mode AFM topography and lateral deflection signal, respectively, showing the substrate roughness and location of the flake. The photon energy-dependent S_G and topographically corrected (see below) S_C maps are shown in Fig S3c and d, respectively.

The spectral evolution of the photoconductivity in Fig S3 mirrors that of the flake 1. The images acquired under dark conditions represent a true dark measurement of this flake as

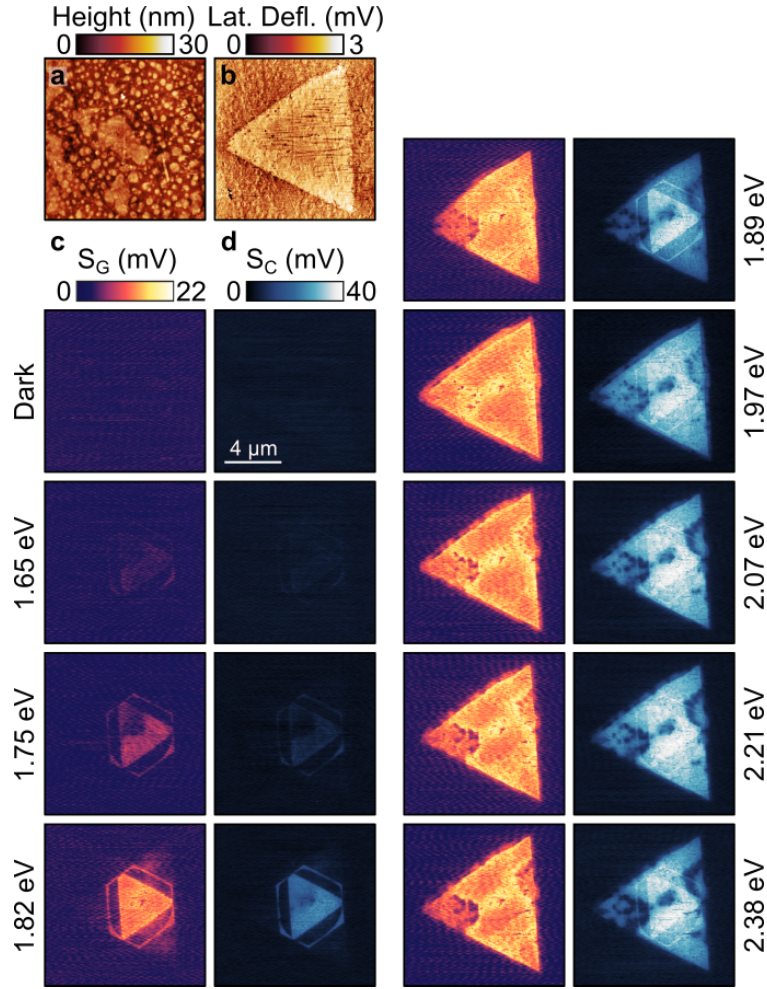


Figure S3: **Photon energy-dependent conductivity of additional flake.** (a) Contact-mode AFM image and corresponding lateral deflection signal (b) of an additional TMD heterostructure flake. The wavelength-dependent evolution of S_G (c) and S_C (d) reveals the structural similarity to flake 1.

it had not previously been measured under illumination. When illuminated, as the photon energy approaches the MoS_2 X_A transition the MoS_2 domain becomes conducting with some weak photoconductivity also observed in the WS_2 domain. As the photon energy is further increased, the photoconductivity in the WS_2 domain approaches that of the MoS_2 domain and little change in the relative signal is seen as the photon energy is further increased above the WS_2 X_A transition. Similar to flakes 1 and 2, regions of reduced photoconductivity are seen throughout, with a particularly prominent feature at the left vertex of the flake. It is notable that these features exhibit lower conductivity throughout this sequence, including

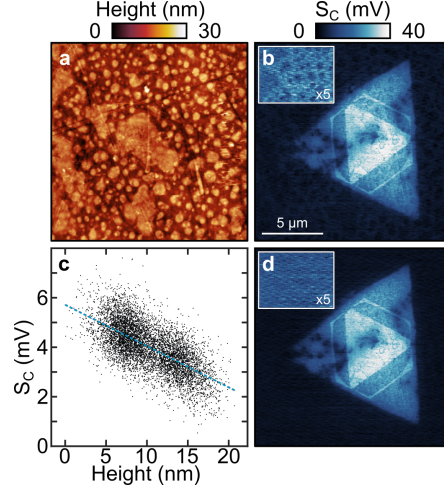


Figure S4: **Correction of capacitive topographic cross-talk.** (a) AFM topography of the TMD heterostructure shown in Figure S3. (b) S_C image taken with 1.89 eV illumination. The intensity of the inset region has been rescaled $\times 5$ to emphasize the topographic cross-talk observed in the S_C channel. (c) A scatter plot for each spatial pixel within the inset region in a and b reveals the correlation between topography and S_C . (d) Corrected S_C image generated by linear regression modeling to the scatter plot in C is free of topographic cross-talk.

at photon energies above the X_A transitions of both materials.

Topographic Correction

Topographic cross-talk into the S_C channel is a well-understood result of the parasitic capacitance between the tip and cantilever body, and the substrate. We correct the topographic cross talk using a statistical approach.³ Shown in Figure S4a is the AFM topography of a TMD heterostructure flake. The corresponding S_C image acquired with 1.89 eV photon energy illumination is shown in Figure S4b, with the inset region rescaled by a factor of 5 to visualize the topographically correlated signal visible over the substrate region. Each spatial pixel in the inset region of Figure S4b is plotted against its corresponding topographic height in the scatter plot shown in c. The obtained linear regression model to the scatter plot (dashed blue line) is used to correct S_C , leaving only residual noise in the corrected image shown in Figure S4d. While the overall contribution of the topographic cross-talk to the

image is comparably weak, we correct all images using this method to optimally measure photoconductivity variations. We also note that the regions of reduced photoconductivity observed throughout all flakes studied here do not generally correlate with topographic variations.

Our measurements are also free of photothermal effects that can arise due to optical illumination and lead to, *e.g.*, thermal expansion of the sample or cantilever that results in corresponding artifacts in S_C . First, we note that our measurements here of photoconductive decay over tens of minutes is significantly longer than any expected thermalization of the cantilever or flake, suggesting that the signal is photoconductive in origin. Furthermore, as S_G is free of parasitic capacitance, it represents the photoconductivity even under illuminated conditions, and the excellent correspondence with S_C show that the measured signal is photoconductive in origin.

Spatial Comparison

Here we examine the spatial correlations between the SMM photoconductivity imaging, the substrate topography, and the optical images. Shown in Figure S5a and b are the S_C image of flake 1 from Figure 2fvi under illumination at a photon energy of 1.97 eV, overlaid with contours of the corresponding contrast-optimized optical image from Figure S2b and AFM topography from Figure 2b, respectively. The equivalent images of flake 2 are shown in Figure S5c and d, with the S_C image from Figure 3eiii overlaid with contours of the contrast-optimized optical image from Figure S2g and AFM topography from Figure 3a, respectively. The overlays in Figure S5a and c confirm the correspondence between the reduced photoconductivity in the S_C and the reduced optical contrast. For the SL regions of flake 2 shown Figure S5c, this agreement is particularly strong, with most regions of reduced conductivity showing some related reduced intensity in the optical images. Since the contrast of the optical image in Figure S2g has been optimized to highlight the SL region,

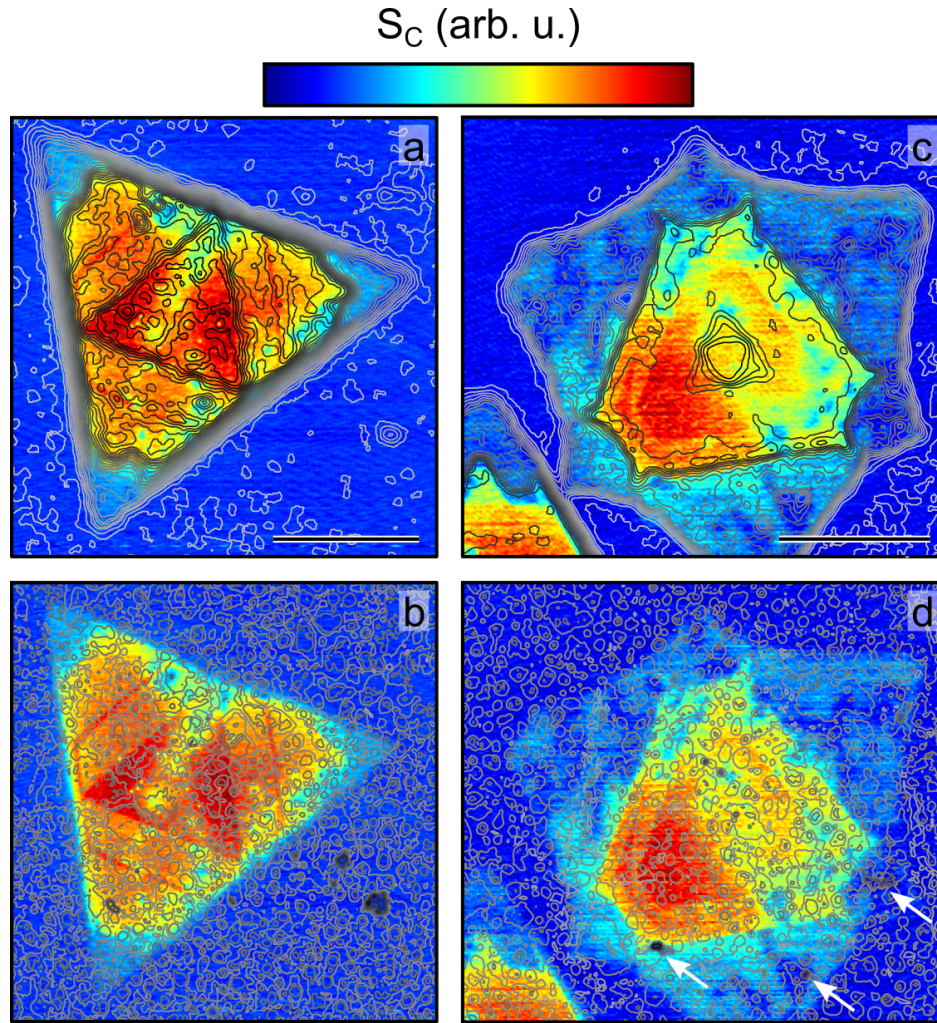


Figure S5: **Overlay of SMM images with AFM topography and optical images.** S_C images of flake 1 taken from Figure 2fvi under illumination with a photon energy of 1.97 eV overlaid with a contour of the contrast-optimized optical image from Figure S2b (a) and the corresponding AFM topography from Figure 2b (b). The equivalent S_C images of flake 2 taken from Figure 3eiii overlaid with a contour of the contrast-optimized optical image from Figure S2g (c) and the corresponding AFM topography from Figure 3b (d). All scale bars are 5 μm and all contour plots are higher/brighter for darker contours.

the agreement in the interior ML regions is weak, though a comparison with the unmodified image in Figure S2f suggests the correspondence in this region is strong. Although the correspondence between the photoconductivity maps and the optical contrast is weaker for the interior ML regions of flake 1 in Figure S5a, many of the low-photoconductivity regions are seen in the optical contours, including small pinhole-like regions in the central ML MoS_2 region.

Unlike the strongly correlated spatial photoconductivity distribution and optical contrast, little correspondence is seen between the photoconductivity and the AFM topography. In particular, the spatial photoconductivity variations do not appear to arise from topographic features, including high or low points, as well as transition regions. The only discernible exceptions are the regions of reduced photoconductivity indicated by white arrows in Figure S5, where tall features are seen. As these features are notably higher than other regions of the substrate, these are likely contaminants and we emphasize that we cannot discern whether these are located underneath or on top of the TMD flake. This indicates that the effect of the sample topography on the observed spatial photoconductivity is weak and suggests other origins. We also note that topographically-induced strain would be expected to be primarily tensile in nature. Tensile strain is reported to result in a bandgap narrowing for both MoS₂⁴ and WS₂.⁵ The reduced bandgap should result in a funneling of free carriers to these regions that results in increased photoconductivity, and they should also be discernible at lower photon energies and result in lower photon energy emission, opposite to what is observed.

Charging and Discharging Kinetics

Here we show the full datasets for the charging and discharging kinetics of flake 2. Shown in Figure S6a is the AFM topography of the flake shown with the corresponding lateral deflection image shown in b. A sequence of S_G and topographically corrected S_C images are shown in Fig S6c and d, respectively. At $t = 0$ min weak conductivity is observed in the multilayer MoS₂ domain, which is residual charging from illumination that was turned off ≈ 14 hours prior. Immediately after this image the flake is illuminated with a photon energy of 1.97 eV. As can be seen, the photoconductivity does not reach steady-state immediately, but after an initial turn-on continues to slowly increase over the 16 minute sequence shown. For all flakes, discernible charging continued even after >60 min of continuous illumination.

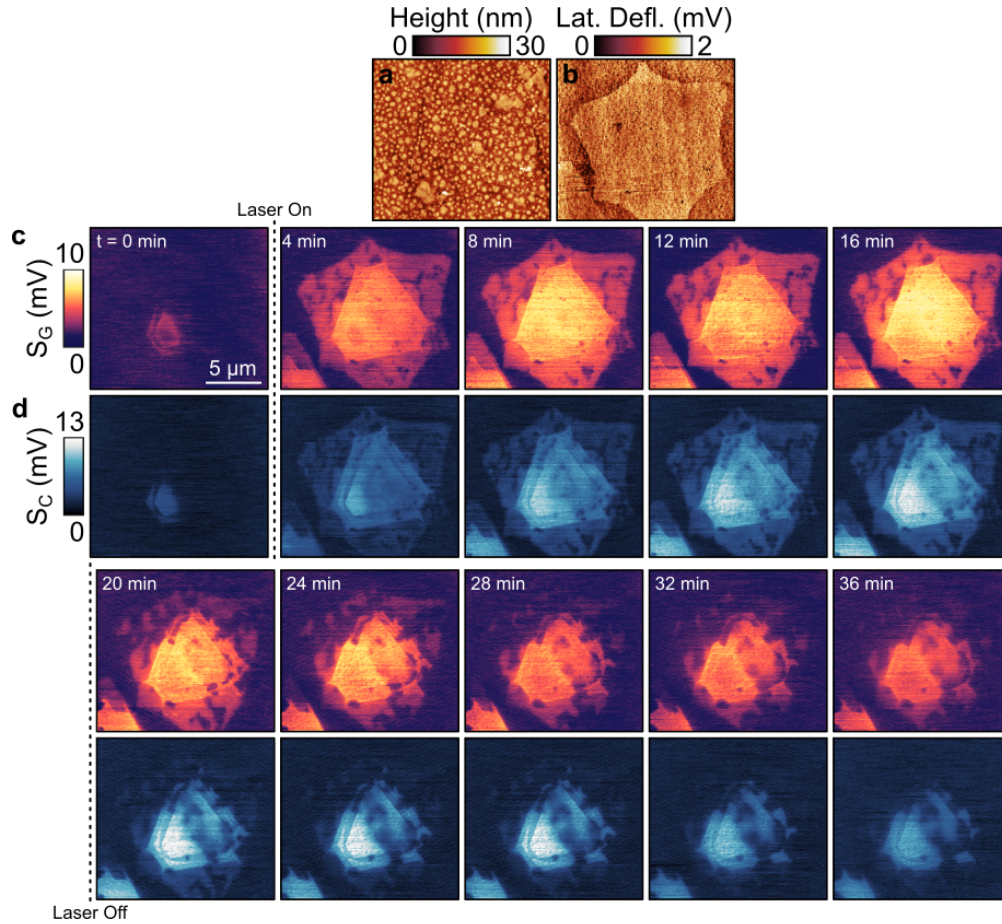


Figure S6: **Photo-induced charging and discharging of flake 2** AFM topography (a) and lateral deflection signal (b) of flake 2. (c) and (d) show the S_G and S_C images, respectively, of the charging and subsequent discharging of the flake in response to illumination as indicated.

After illuminating the sample for 16 minutes we turn off the illumination in this sequence to observe the discharging. The conductivity decays significantly faster over the monolayer WS_2 domain than the multilayer domains. Other significant and highly reproducible features become apparent as well. For instance, the region in the interior of the flake where residual charge is initially visible, charges rapidly and reaches the highest conductivity of any region in the flake as evidenced by the S_C images. This region also discharges significantly slower than other regions within the flake, suggesting consistent long-term persistence of free carriers in this region. Similarly, there are regions throughout the sample that charge slowly, attain lower photoconductivity than surrounding regions comprised of the same material

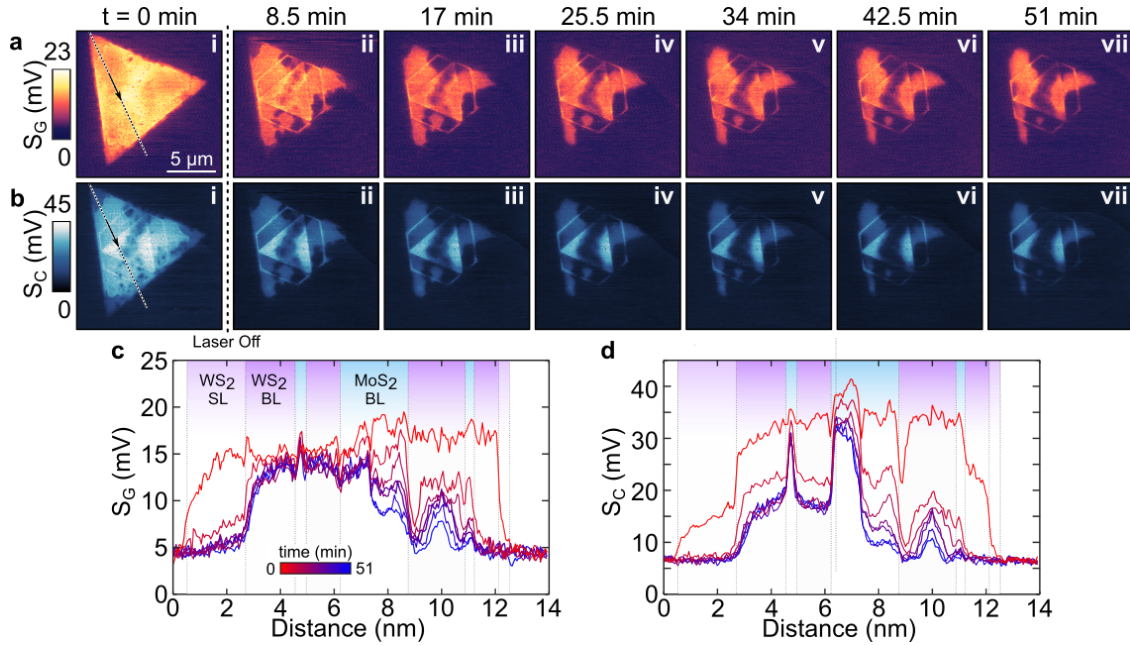


Figure S7: **Decay of persistent photoconductivity in flake 1** A sequence of S_G (a) and S_C (b) images showing the photoconductivity decay at times indicated after the optical illumination is turned off. Line cuts along the dashed lines in Ai (c) and Bi (d), respectively.

and thickness, and discharge much more rapidly. It is important to note that such spatial variations are highly reproducible and seen for all flakes studied.

Shown in Figure S7 are a sequence of images showing the photoconductivity decay of flake 1. Also shown are line cuts of S_C and S_G taken along the dashed lines in i to illustrate the varying rates of decay in the different regions.

Sample Charging

In order to verify that hot electron injection⁶ is not responsible for the observed photoconductivity and associated sample charging we performed additional measurements. Shown in Figure S8 are a set of S_G (a and b) and S_C images (c and d) showing the photoconductivity decay after sample illumination was turned off. The images in Figure S8a and c correspond to the scans shown in Figure S7, where the sample was repeatedly scanned with the tip in contact during sample illumination. In contrast, for the figures in Figure S8b and d the sam-

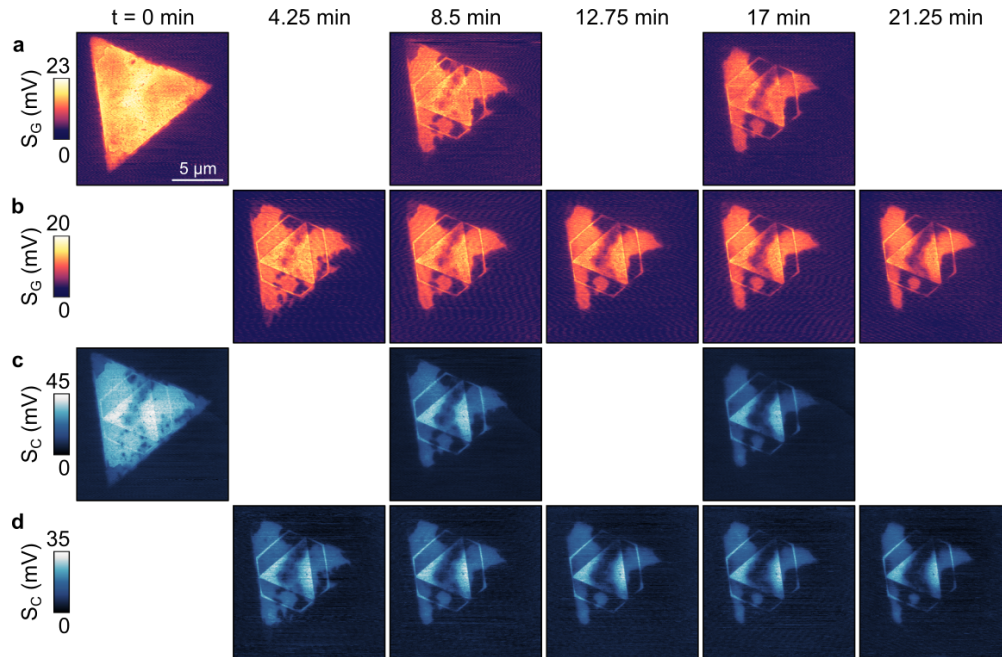


Figure S8: **Verification of lack of charge transfer from tip** S_G images (a) and (b) and S_C images (c) and (d) showing the photoconductive decay of flake 1. (a) and (c) correspond to the images in Figure 7 while in (b) and (d) the tip was retracted prior to illumination and re-engaged only after illumination was turned off.

ple was first kept under dark conditions for >7 days. Prior to illumination the sample was then scanned to verify the flake position and the tip then retracted by $\approx 3 \mu\text{m}$. The sample was then illuminated for 20 minutes, and we re-engaged the tip only after the illumination was turned off.

The temporal sequences shown in Figure S8 show a remarkably similar spatial distribution of residual charge and its persistence. These two sets of decay sequences clearly show that the observed spatial photoconductivity and long-term discharging kinetics result from sample properties and are not significantly affected by the presence of the tip. It is important to note that our Pt tips do not support localized plasmonic resonances in the visible spectral range. This limits the local field enhancement, and charge transfer is not favored by the weak tip-perpendicular (in the sample plane) optical fields used here.

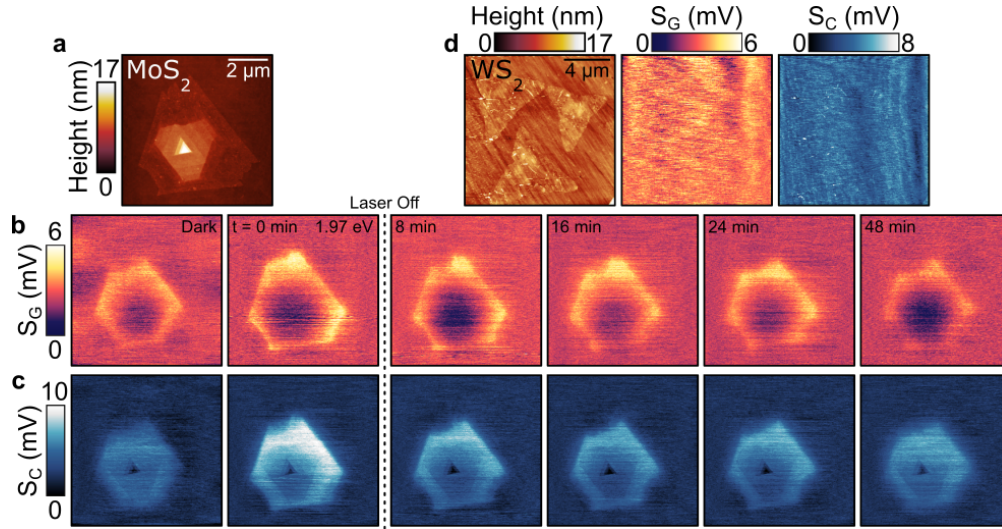


Figure S9: **Photoconductivity of individual MoS₂ and WS₂ lateral heterojunctions** AFM topography (a) and a sequence of S_G (b) and S_C (c) scans of a MoS₂ multilayer heterojunction. For the MoS₂ the photoinduced charging and subsequent discharging can be clearly seen, while the WS₂ multilayer heterojunction (d) shows no appreciable photoconductivity and charging even under resonant excitation with a photon energy of 1.97 eV.

Multilayer Heterojunctions

In order to better understand the persistent photoconductivity observed in the lateral heterostructures we independently examine individual multilayer heterojunctions of MoS₂ and WS₂. In Figure S9 we show results from these multilayer heterojunctions, grown by chemical vapor deposition and transferred to quartz using a polystyrene stamp transfer.

The contact mode AFM topography of the MoS₂ flakes as shown in Figure S9a shows a well-defined structure with thickness ranging from single layer at the edges to a thickness of 17 nm at the center. In the corresponding S_G and S_C images b and c, respectively, we see that under dark conditions the thicker interior regions have significant dark conductivity. Upon illumination with a photon energy of 1.97 eV, photoconductivity emerges in the thinner exterior regions, though the conductivity of the single layer region at the edge remains below the detection threshold. When we turn off the illumination a residual photoconductivity remains that then decays over time. This persistent photoconductivity is analogous to that observed in the lateral heterojunctions.

In contrast to the MoS₂ lateral heterojunctions, WS₂ structures show neither appreciable conductivity nor photoconductivity. Shown in Figure S9d are the AFM topography showing a small cluster of WS₂ with thickness ranging from single layer up to ≈ 10 nm as well as the corresponding S_G and S_C images acquired with 1.97 eV photon energy illumination under conditions identical to those in c. Although some scanning-related artifacts are seen in both the S_G and S_C channels, there is no discernible photoconductivity over any region of the flakes examined. It is worth emphasizing that unlike MoS₂ flakes, the WS₂ flakes did not show any dark conductivity either.

References

- (1) Sahoo, P. K.; Memarian, S.; Xin, Y.; Balicas, L.; Gutiérrez, H. R. One-Pot Growth of Two-Dimensional Lateral Heterostructures *via* Sequential Edge-Epitaxy. *Nature* **2018**, *553*, 63–67.
- (2) Sahoo, P. K.; Memaran, S.; Nugera, F. A.; Xin, Y.; Márquez, T. D.; Lu, Z.; Zheng, W.; Zhigadlo, N. D.; Smirnov, D.; Balicas, L.; Rodríguez Gutiérrez, H. Bilayer Lateral Heterostructures of Transition-Metal Dichalcogenides and Their Optoelectronic Response. *ACS Nano* **2019**, *13*, 12372–12384.
- (3) Coakley, C. J.; Berweger, S.; Wallis, T. M.; Kabos, P. Disentangling Topographic Contributions to Near-Field Scanning Microwave Microscopy Images. *Ultramicroscopy* **2019**, *197*, 53–64.
- (4) Castellanos-Gomez, A.; Roldán, R.; Cappelluti, E.; Buscema, M.; Guinea, F.; van der Zant, H. S. J.; Steele, G. A. Local Strain Engineering in Atomically Thin MoS₂. *Nano Lett.* **2013**, *13*, 5361–5366.
- (5) Shen, T.; Penumatcha, A. V.; Appenzeller, J. Strain Engineering for Transition Metal Dichalcogenide Based Field Effect Transistors. *ACS Nano* **2016**, *2016*, 4712–4718.

- (6) Tang, C.; He, Z.; Chen, W.; Jia, S.; Lou, J.; Voronine, D. Quantum Plasmonic Hot-Electron Injection in Lateral WSe₂/MoSe₂ Heterostructures. *Phys. Rev. B* **2018**, *98*, 041402(R).